Charge ordering in magnetite at low temperatures

J. M. Zuo and J. C. H. Spence
Physics Department, Arizona State University, Tempe, Arizona 85287

W. Petuskey
Chemistry Department, Arizona State University, Tempe, Arizona 85287
(Received 21 June 1990)

The ordering of the Fe^{2+} and Fe^{3+} ions on the octahedral sites of magnetite (Fe_3O_4) at temperatures below the Verwey metal-insulator transition has been studied by quantitative high-energy transmission electron diffraction. We find that there are ten independent charge-ordering models (including the Verwey model) for the low-temperature structure that satisfy the Anderson condition if the symmetry is *Cc* (monoclinic). Dynamical electron diffraction patterns are simulated and compared with experiment for these charge-ordering models, using atomic coordinates obtained from neutron diffraction work. We find that one of these ten charge-ordering models agrees best with experiment and that the electrons in this model form a characteristic wave. Our calculations of electron correlation energy show that this model has the second lowest energy, while the Verwey model has the lowest. This indicates the importance of electron-phonon interactions in stabilizing the structure.

I. INTRODUCTION

Magnetite (Fe_3O_4) undergoes a metal-insulator transition (the so-called Verwey transition) near 120 K,[1,2] the nature of which has been the subject of continuous interest. Verwey, Haayman, and Romeijn[2] first proposed that the transition is due to the ordering of the Fe^{2+} and Fe^{3+} ions on the octahedral sites of magnetites' inverse spinel structure. They also suggested that above the transition temperature the material conducts by electron hopping between the octahedral sites. Their charge-ordering model (usually called the Verwey model) was thought to be confirmed by Hamilton in 1958 (Ref. 3) who first observed the $(002)_c$ magnetic reflection. However, first, in the 1970's, electron-[4] and neutron-diffraction[5] experiments revealed the existence of half-integer reflections, i.e., $(h,k,l+\frac{1}{2})$ (cubic indexing), indicating a doubling of the *c* axis. Other reflections, which are otherwise forbidden above T_c, have also been observed. Second, the neutron-diffraction measurements of Shirane *et al.*[6] proved that the $(002)_c$ magnetic scattering is actually zero if the contribution from simultaneous reflection is removed. Third, Mössbauer[7] and NMR (Refs. 8 and 9) measurements have identified more different Fe^{2+} and Fe^{3+} sites than the single Fe^{2+} and single Fe^{3+} sites predicted by the Verwey model. The NMR experiment of Mizugouchi[9] identified five different Fe^{3+} sites on the octahedral sites. Of these three experimental results, the Mössbauer and NMR results provide the most direct evidence against the Verwey model. However, the idea of charge ordering on the octahedral sites was confirmed by Mössbauer experiments,[7,8] which found that below T_c the Fe^{2+} only occurs on the octahedral sites, and the Fe^{2+} and Fe^{3+} can be clearly distinguished. On the other hand, the idea of a pure charge-ordering transition mechanism was called into question by the measurements of Fuji *et al.*[10] using neutron critical scattering, which showed that the Verwey transition is coupled with a lattice instability characterized by Δ_5 symmetry with a wave vector $\mathbf{q}=(0,0,\frac{1}{2})$ (cubic indices). Theoretically it has been proposed that the low-temperature structure is due to small or intermediate polaron ordering,[11] while Yamada[12] showed evidence of a general lattice instability due to electron-phonon coupling. Specifically he showed the importance of the Δ_5 phonons at $\mathbf{q}=(0,0,\frac{1}{2})$ in magnetite. More recently, approximate atomic displacements have been measured below the transition temperature using neutron diffraction by Iizumi *et al.*,[13] from which they showed that these displacements are mainly due to the condensation of Δ, Z, and Γ phonons. Attempts to refine a charge-ordering model from the same neutron-scattering data set failed because neutron scattering is more sensitive to atomic displacements than to charge ordering.[13] A number of new charge-ordering models have also been proposed, based on recent experimental or theoretical results,[9,12,14,15] especially the NMR results of Mizugouchi.[9,14] However, none of these models can explain all the existing experimental evidence. They either do not agree with the NMR results or with the measured symmetry of the crystal.

In summary, the atomic positions below the transition temperature are now approximately known, while the Verwey model has been disproved. The ionic arrangement remains unknown. The reason for this is mainly due to the insensitivity of x-ray or neutron diffraction to the small changes in charge distribution that result from electron ordering. The interpretation of these experimental results is further complicated by the existence of multiple twins in the low-temperature structure.

The symmetry of the low-temperature structure has

been found to be *Cc* (monoclinic) by x-ray diffraction[16] and neutron diffraction.[17] However, Rado and Ferrari[18] and Shiratori *et al.*[19] have observed the magnetoelectric effect, which implies that the space group is $P1$. Recently, however, the *Cc* space group has been confirmed by convergent-beam electron diffraction (CBED) by Tanaka,[20] who observed dynamically forbidden reflections due to the *c*-glide symmetry. In this paper we will show additional evidence of *Cc* symmetry. Since electron diffraction is very sensitive to the charge distribution and to small symmetry changes, we believe that the symmetry is *Cc*. Several previously proposed charge-ordering models do not have *Cc* symmetry, except the Verwey model, which has higher symmetry. With *Cc* symmetry the complexity of the problem is reduced fourfold, however, there remain many possibilities.

Another key to understanding the structure is provided by the Anderson condition.[21] This condition requires that in every tetrahedron formed by the octahedral sites of the spinel structure there are two Fe^{2+} and two Fe^{3+} ions, due to the strong Coulombic interaction between electrons. With *Cc* symmetry and the Anderson condition combined, we find that there are ten independent ionic arrangements, one of which is the Verwey model. The final experimental result with which models must be consistent is the NMR finding that there are five inequivalent Fe^{3+} sites on the octahedral sites.[9] Several of the ten independent models have five or more different Fe^{3+} nearest-neighbor configurations. However, none of these satisfy the additional assumptions of Mizugochi.[22] New experimental evidence is therefore needed to distinguish the possible models.

We have used convergent-beam electron diffraction (CBED) to determine the charge ordering. Low-angle transmission electron diffraction is well known for its sensitivity to electron distributions. For example, by accurately measuring low-order structure factors, the bonding electron distribution in GaAs has recently been measured.[23] In addition, the electron probe can be focused down to a few nanometers in diameter, while the sample is being imaged. A single domain of perfect crystal can therefore be selectively studied. Unlike x-ray diffraction, however, electron diffraction has so far been unsuccessful in solving unknown periodic structures, except in a very few cases (for a review, see Ref. 24). This is mainly due to the strong multiple scattering of electrons that results from the strong interaction of electrons with matter. In consequence, the intensity of scattered electron beams is not simply related to structure factor amplitudes, as for x rays.

These properties of electrons make them ideal for the study of the low-temperature structure of magnetite as follows. First, we note that this structure only differs from the high-temperature cubic structure by very small atomic displacements, and a redistribution of $\frac{1}{110}$ electrons. Second, the reflections can be divided into strong "high-temperature" and weak "low-temperature" reflections. The low-temperature reflections are due to a small departure from the cubic structure, which disappears above T_c. We will show that, at low temperature, the high-temperature reflections can be approximated by the cubic structure, and that they are responsible for the main multiple-scattering interactions. To a good approximation, the low-temperature reflections can be neglected at first. This allows the refinement of diffraction parameters such as the thickness and the incident-beam direction from the high-temperature reflections. With these parameters known, the intensity of the low-temperature reflections can be simulated accurately. In this paper, we compare the simulated intensity of several model-sensitive low-order reflections in the [001] zone with experimental ones for all the independent charge-ordering models under space group *Cc*, and further restricted by the Anderson condition. We will show that one particular charge-ordering model agrees best with our experiment results and may explain the existing experimental results.

II. THE STRUCTURE OF MAGNETITE

Magnetite $[Fe^{3+}(Fe^{2+}Fe^{3+})O^{2-}{}_4]$ is a ferrimagnet, which has the inverse spinel structure AB_2O_4 above the transition temperature (120 K). The cubic cell ($a=8.3963$ Å) (Ref. 25) contains 8 formula units (f.u.). The atoms occupy the special positions of 8(*a*), 16(*d*), and 32(*e*) in the $Fd3m$ space group. The (*a*) position (the tetrahedral *A* site) is occupied by Fe^{3+} ions, while the (*d*) positions (the octahedral *B* site) are randomly occupied by Fe^{2+} and Fe^{3+}. The (*e*) site is occupied by oxygen. Figure 1 shows a picture of the spinel structure. The whole structure can be understood in a simple way. The oxygen lattice has an almost perfect fcc close-packed structure (position parameter $u=0.379$, but $u=0.375$ if perfect).[2] Each cubic spinel cell contains eight oxygen fcc cells. The *A* site, occupied by Fe^{3+}, is the tetrahedral interstitial site of the oxygen fcc structure, while the *B*

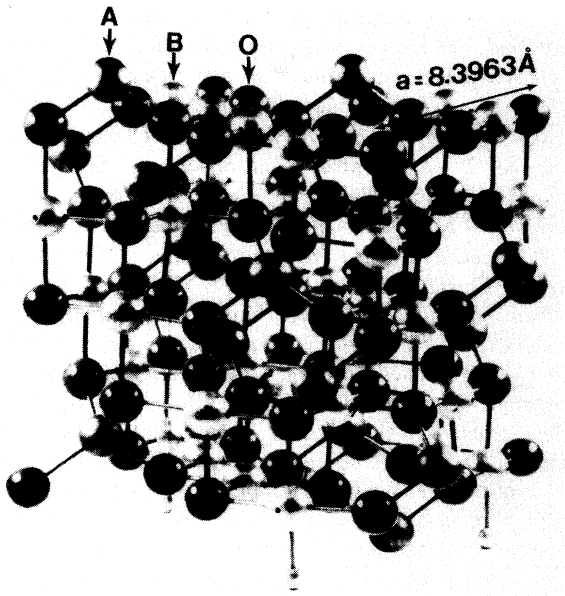

FIG. 1. Model of the spinel structure. This model contains one cubic unit cell. The *A* site, *B* site, and oxygen in this model are indicated by arrows.

site, occupied by randomly distributed Fe^{2+} and Fe^{3+} ions, is the octahedral interstitial site of the oxygen lattice. The A sites form a diamond lattice. The B-site structure (on which the charge ordering occurs) is more complicated, but it has two characteristics. First, the nearest-neighbor B sites form strings that run in different [110] directions. These strings form separate planes, each plane containing only strings running in the same direction. Second, the nearest-neighbor B sites form a tetrahedron. The whole B-site structure can be constructed by linking alternate corners of a tetrahedron, as shown in Fig. 2. The centers of the tetrahedra also form a diamond lattice.

The kinematical reflection conditions (giving allowed reflections) for the oxygen, A- and B-site lattices are given below, using cubic indices:

for oxygen, hkl: $h+k,h+l,k+l=2n$,

$0kl$: $k+1=4n$ and $k,l=2n$,

hhl: $h+l=2n$,

$h00$: $h=4n$,

or (1)

hkl: $h+k,h+l,k+l=4n$ if the oxygen atom's small departure from perfect fcc packing is neglected ;

for the A site, hkl: $h,k,l=2n+1$ or $h+k+l=4n$;

for the B site, hkl: $h,k,l=2n+1$ or $h,k,l=4n+2$ or $h,k,l=4n$.

For the complete crystal, satisfying any one of the above conditions generates an allowed reflection, since all three sublattices have different structures. The remaining reflections are kinematically extinct. Some of these, due to screw or glide elements, may remain extinguished for all thicknesses (despite multiple scattering) for certain incident-beam directions. Others are absent due to our choice of nonprimitive cell. These "dynamical forbidden" will be discussed later for the particular diffraction condition used in this experiment.

Below the transition temperature, the structure is monoclinic and the unit cell contains four rhombohedrally distorted cubic cells.[26,13] The relationship between the low-temperature cell and the rhombohedral distorted cubic cell is shown in Fig. 3. The unit cell is defined by

$$\mathbf{a}_m=-\mathbf{a}_R-\mathbf{b}_R\ ,$$
$$\mathbf{b}_m=\mathbf{a}_R-\mathbf{b}_R\ , \qquad (2)$$
$$\mathbf{c}_m=2\mathbf{c}_R\ ,$$

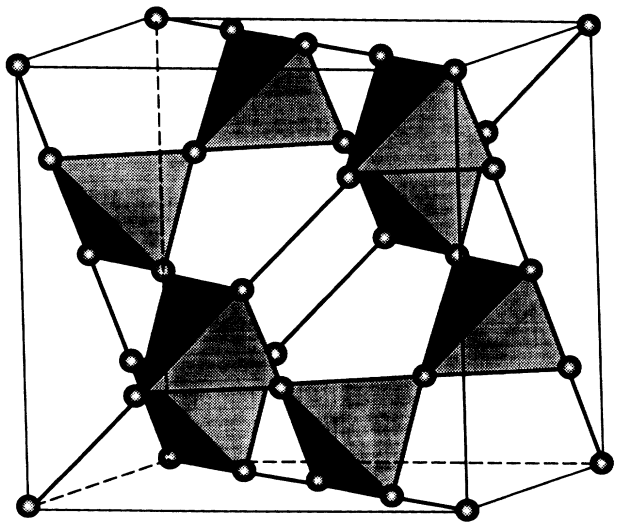

FIG. 2. The B-site structure of spinel structure. The A site and oxygen are not shown. The nearest-neighbor B sites form a tetrahedron. These tetrahedra are linked together by alternate corners, and the centers of the tetrahedra form a diamond lattice. The nearest-neighbor B sites form a string in $\langle 110\rangle$ directions.

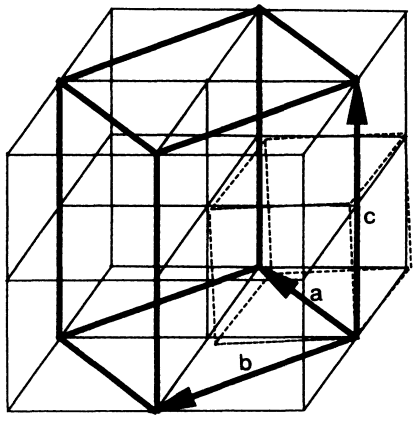

FIG. 3. The relations between the low-temperature monoclinic unit cell (double lines) and the rhombohedral distorted cubic cell (solid lines), and the high-temperature cubic cell (dashed lines) of magnetite. The low-temperature monoclinic unit cell contains four rhombohedral distorted cubic cells. In the monoclinic cell, the c axis is doubled. The b axis is along the $[1\bar{1}0]$ direction of the cubic cell and is perpendicular to a and c axes.

with $a_m = 11.868(2)$, $b_m = 11.851(2)$, $c_m = 16.752(4)$ Å, and $\beta = 90.20°$.[13] Here m denotes the monoclinic cell and R denotes the rhombohedral distorted cubic cell. In this paper we will use the monoclinic indices (h_m, k_m, l_m) with the footnote m neglected unless otherwise specified. The relations between the monoclinic indices and cubic indices are given by

$$h_c = (-h_m + k_m)/2 ,$$
$$k_c = -(h_m + k_m)/2 , \quad (3)$$
$$l_c = l_m/2 .$$

Experimentally, two types of kinematically forbidden reflections were observed in x-ray[16] and neutron diffraction[17] at low temperatures. One is the absence of the $(h00)$ and $(k00)$ reflections with $h,k = 2n+1$, indicating C centering. The other is the absence of $(h,0,l)$ with $l = 2n+1$, indicating a c-glide element. No other symmetry was observed. These two types of absence are easily seen in the low-temperature electron diffraction pattern of Fig. 4. Figure 4 shows the CBED pattern from the [001] zone axis that clearly shows the absence of the $(h00)$ and $(0k0)$ reflections with $h,k = 2n+1$. Figure 4 also shows the absence of the kinematically forbidden reflection $(\pm 20,0,1)$ due to the c glide in the first Laue zone as indicated by the arrow. This reflection remains absent despite multiple scattering because the coupled high-order Laue zone (HOLZ) reflections are very weak. Additional evidence for the c glide has been reported by Tanaka.[20] He observed dynamically forbidden reflections (known as Gjonnes-Moodie[27] lines) due to the c-glide element, and no other symmetry.

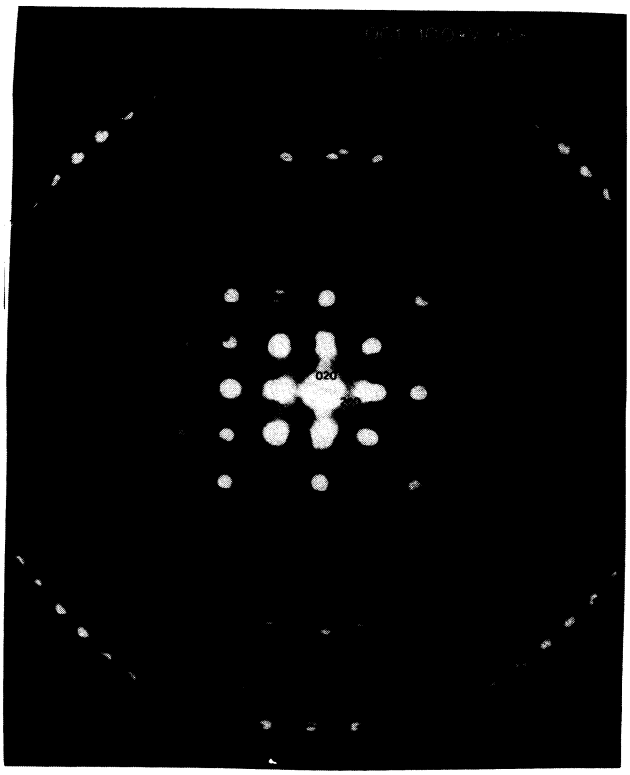

FIG. 4. Convergent-beam electron diffraction pattern of low-temperature magnetite near the [001] zone axis. This CBED pattern was recorded at 100 kV with a sample temperature of 90 K. The $(2n+1,00)$ and $(0,2n+1,0)$ reflections are missing, indicating c centering. The first-order Laue zone due to c-axis doubling is shown. The missing $(\pm 20,0,1)$ reflections due to the c glide are indicated by arrows.

Rado and Ferrari[18] and Shiratori *et al.*[19] have observed the magnetoelectric effect. These measurements show that the structure is noncentrosymmetric with a small departure from the c glide. Their result implies the $P1$ space group. Iizumi *et al.*[13] showed that if there are displacements that violate the c-glide symmetry, they are very small and beyond current experimental accuracy. Tanaka's result, and our electron-diffraction results indicate that the charge ordering also has Cc symmetry, since low-order electron-diffraction reflections are very sensitive to the charge distribution (unlike x rays or neutrons). Hence the low-temperature structure space group is monoclinic Cc within the accuracy of current diffraction experiments.

The atomic positions below the transition temperature have been measured by Iizumi *et al.*[13] at 10 K using neutron diffraction. The measurement was carried out by standard refinement procedures, in which the atomic positions and Debye-Waller factors are adjustable parameters. Their results, which we use for our electron-diffraction measurements are shown in Table I. Unfortunately a reduced cell was used (the a and b axes halved) with higher symmetry ($Pmc2_1$ for our data set) than Cc. Hence their results gave "averaged" approximate atomic positions. The reason for this is that the low-temperature structure of magnetite has a high degree of pseudosymmetry, because the atomic shifts are very small so that cubic symmetry is approximately retained. Iizumi *et al.*[13] showed that the dominant part of the atomic displacements at low temperature are due to the condensation of Δ $[\mathbf{q} = (0,0,\frac{1}{2})_c]$, Z $[\mathbf{q} = (0,0,1)_c]$, and Γ $[\mathbf{q} = (0,0,0)]$ phonons, while the W $[\mathbf{q} = (1,0,\frac{1}{2})_c]$ or $\mathbf{q} = [0,1,1\frac{1}{2})_c]$ and X $[\mathbf{q} = (1,0,0)_c$ or $\mathbf{q} = (0,1,0)_c]$ phonons have much weaker contribution. (Here c denotes cubic indexing.)

III. CHARGE ORDERING WITH *Cc* SYMMETRY

Symmetry Cc has two symmetry components: base centering on the a-b plane and a c-glide element, with a-c as the glide plane and the c axis as the glide direction. These two symmetry operations give a total of four symmetry related positions. The low-temperature monoclinic cell has a total of 64 B sites, which is reduced to 16 independent B sites by Cc symmetry. The distribution of these 16 independent B sites in the unit cell is shown in Fig. 5, in which only B sites are shown and the oxygen and A sites deleted. As shown in the figure, the low-temperature unit cell can be described as $ABA'B'A''B''A'''B'''$ stacking. All A-type planes have B-site strings along the a axis and all B type planes have B-site strings along the b axis. The 16 independent B sites are distributed equally in the first four planes. Symmetry related positions are also shown in Fig. 5. To con-

TABLE I. The low-temperature atomic coordinates and Debye-Waller factors measured by neutron diffraction (Ref. 13). Under *Cc* symmetry, there are eight independent *A* sites, 16 independent *B* sites, and 32 independent oxygen positions. These positions and position dependent Debye-Waller factor are listed in this table. Cell constants are $a_m = 11.868(2)$, $b_m = 11.851(2)$, $c_m = 16.752(4)$ Å, and $\beta = 90.20$ (Ref. 13).

Site	x	y	z	B	Site	x	y	z	B
A(1)	0.25	0.003 25	0.064	0.05	*A*(2)	0.25	0.503 25	0.064	0.05
A(3)	0.25	0.254 35	0.1891	0.08	*A*(4)	0.25	0.754 35	0.1891	0.08
A(5)	0.0	0.2522	0.3117	0.08	*A*(6)	0.0	0.7522	0.3117	0.08
A(7)	0.0	0.0013	0.437	0.05	*A*(8)	0.0	0.5013	0.437	0.05
B(1)	0.126 95	0.251 35	0.9998	0.13	*B*(2)	0.373 05	0.251 35	0.9998	0.13
B(3)	0.626 95	0.251 35	0.9998	0.13	*B*(4)	0.873 05	0.251 35	0.9998	0.13
B(5)	0.0	0.129 85	0.1213	0.10	*B*(6)	0.0	0.380 15	0.1263	0.01
B(7)	0.0	0.629 85	0.1213	0.10	*B*(8)	0.0	0.880 15	0.1263	0.01
B(9)	0.121 65	0.0049	0.2476	0.14	*B*(10)	0.378 35	0.0049	0.2476	0.14
B(11)	0.621 65	0.0049	0.2476	0.14	*B*(12)	0.878 35	0.0049	0.2476	0.14
B(13)	0.25	0.134	0.3787	0.10	*B*(14)	0.25	0.3752	0.3753	0.01
B(15)	0.25	0.634	0.3787	0.10	*B*(16)	0.25	0.8752	0.3753	0.01
O(1)	0.0	0.1242	0.0012	0.13	O(2)	0.0	0.6242	0.0012	0.13
O(3)	0.0	0.371 95	0.002	0.16	O(4)	0.0	0.871 95	0.002	0.16
O(5)	0.122 45	0.253 35	0.1239	0.11	O(6)	0.377 55	0.253 35	0.1239	0.11
O(7)	0.122 45	0.753 35	0.1239	0.11	O(8)	0.377 55	0.753 35	0.1239	0.11
O(9)	0.120 35	0.004 25	0.1291	0.17	O(10)	0.120 35	0.504 25	0.1291	0.17
O(11)	0.379 65	0.004 25	0.1291	0.17	O(12)	0.379 54	0.504 25	0.1291	0.17
O(13)	0.0	0.1178	0.2464	0.27	O(14)	0.0	0.617	0.2464	0.27
O(15)	0.0	0.388 05	0.2492	0.20	O(16)	0.0	0.888 04	0.2492	0.20
O(17)	0.25	0.3819	0.2549	0.20	O(18)	0.25	0.8819	0.2549	0.20
O(19)	0.025	0.128 15	0.2555	0.27	O(20)	0.25	0.628 15	0.2555	0.27
O(21)	0.132	0.0048	0.3706	0.17	O(22)	0.368	0.0048	0.3706	0.17
O(23)	0.132	0.5048	0.3706	0.17	O(24)	0.368	0.5048	0.3706	0.17
O(25)	0.128 75	0.2521	0.3755	0.11	O(26)	0.371 25	0.2521	0.3755	0.11
O(27)	0.128 75	0.7521	0.3755	0.11	O(28)	0.371 25	0.7521	0.3755	0.11
O(29)	0.25	0.3657	0.4968	0.16	O(30)	0.25	0.8657	0.4968	0.16
O(31)	0.26	0.128	0.4994	0.13	O(32)	0.25	0.628	0.4994	0.13

struct a charge-ordering model, we distribute eight Fe^{2+} and eight Fe^{3+} over these 16 positions, giving about 5×10^8 possibilities. The Anderson condition provides another constraint.[21] This states that in every tetrahedron formed by nearest-neighbor *B* sites there are two Fe^{2+} ions and two Fe^{3+} ions. This is based on the fact that the energy gained by long-range ordering is only about 5% of the energy gained by the Anderson short-range ordering. This fact is also shown in our calculation of the Coulomb electron correlation energy for different charge-ordering models (see Sec. VI). The energy difference between different charge-ordering models is about 5 to 10% of the energy of short-range ordering. This Anderson condition is consistent with the requirement that the Pauling electrostatic bond strength (EBS) should be as close as possible to 2. Here we define EBS as cation valence divided by coordination number.[28] If all nearest-neighbor arrangements around the oxygen site are considered, the two best arrangements that can be found give EBS values of $2\frac{1}{6}$ and $1\frac{5}{6}$. These have (a) two Fe^{3+} on a octahedral site, one Fe^{2+} on a octahedral site, and one Fe^{3+} on a tetrahedral site, and (b) two Fe^{2+} on a octahedral site, one Fe^{3+} on a octahedral site, and on Fe^{3+} on a tetrahedral site. For the octahedral sites, these arrangements require that no one tetrahedral face has all the same Fe valence, and hence the Anderson tetrahedral unit is obtained.[29] There is some experimental evidence of the Anderson short-range ordering below and above the transition temperature by Mössbauer[30] and heat measurements.[31] With the Anderson condition and *Cc* symmetry, there are three ways of filling the *B*-site planes with Fe^{2+} and Fe^{3+}: (1) Zero (or four) Fe^{3+} ions on the *A* plane, four (or zero) Fe^{3+} on the *B* plane (Verwey model[2]). (2a) One Fe^{3+} on the *A* plane, three on the *B* plane, or (2b) three Fe^{3+} on the *A* plane and one on the *B* plane. (3) Two Fe^{3+} ions on the *A* plane and two on the *B* plane.

We will call the possibilities (2a), (2b), and (3) the 1-3, 3-1, and 2-2 fillings, respectively. Since the Verwey model has been disproved, we need only consider possibilities (2) and (3). There are 16 ways to fill the 16 independent *B* sites alone under 1-3 filling. However, not all of them are independent—by shifting origin and inversion (neglecting the small monoclinic distortion) we are able to reduce these 16 models to two independent ones. By considering all possibilities under (2) and (3), we find a total of nine independent charge-ordering model. These nine models plus the Verwey model are listed in Table II. In Table II, models 1 and 2 are given under the 1-3 filling, models 3 and 4 under 3-1 filling, models 5–9 under 2-2 filling, and

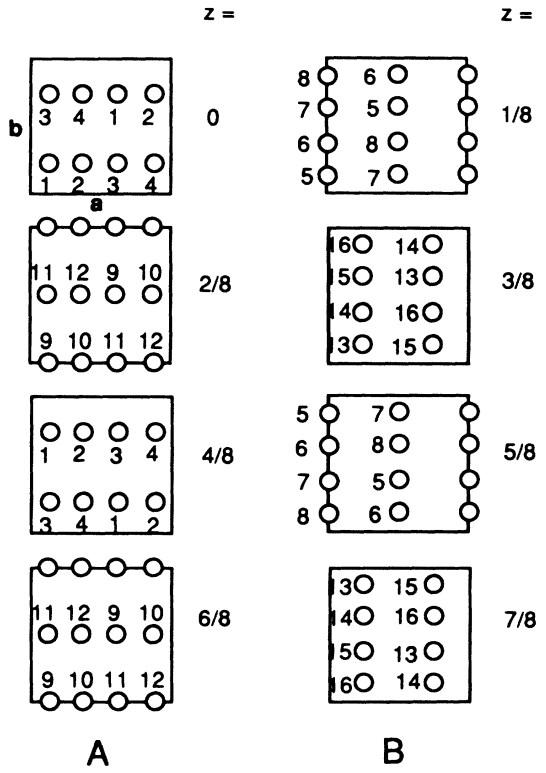

FIG. 5. The *Cc* symmetry related *B*-site positions in the low-temperature magnetite structure. There are 16 independent *B* sites with *Cc* symmetry. These 16 *B* sites are marked by numbers 1–16 in this figure. Low-temperature magnetite consists of a stacking of four *A* type and four *B* type planes in the sequence $ABA'B'A''B''A'''B'''$. The *A* and *B* planes contain *B*-sites strings in the *a* and *b* directions, respectively. Each plane (with *z* coordinate) is shown. The 16 independent *B* are distributed equally over the first four planes.

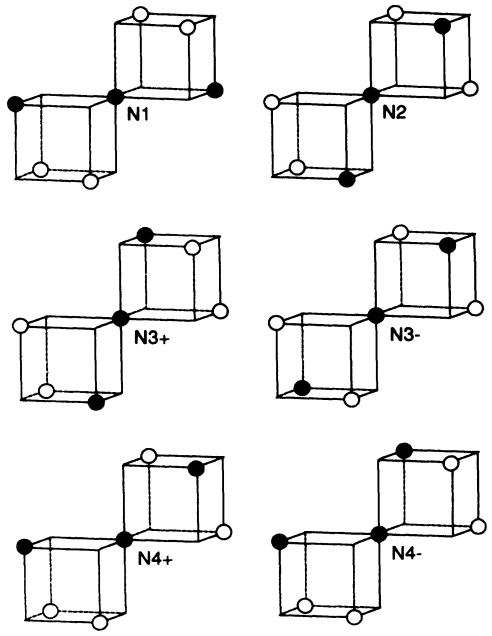

FIG. 6. The six possible nearest-neighbor Fe^{3+} (solid circle) configurations, labeled $N1$, $N2$, $N3\pm$, and $N4\pm$. The $N3+$ and $N4+$ arrangements are related to the $N3-$ and $N4-$ by mirror operations, respectively.

models 10 and 11 are the Verwey models. Model 6 has been proposed by Yamada and co-workers.[4] If we also consider the coupling between charge ordering and atomic displacements, then every possible model is independent in terms of the way it is coupled with the atomic displacement. However, our structure factor calculations show that the difference between different types of charge ordering is much larger than the difference between different couplings of the same charge ordering. The current experiment is not sufficiently accurate to resolve differences due to different couplings. In this paper, we concentrate on the problem of charge ordering.

These charge-ordering models must be consistent with the experimental NMR results,[9,14] which show five different Fe^{3+} sites on the *B* site. Following the assumption by Mizugouchi[14] that the magnetic field on Fe^{3+} is determined by the nearest-neighbor Fe^{3+} configuration, there are six nearest-neighbor configurations under the Anderson condition and assuming inversion symmetry of

TABLE II. The 11 independent charge-ordering models under *Cc* symmetry and the Anderson condition. In this table the Fe^{2+} and Fe^{3+} distribution in the 16 independent *B* sites are shown for every model. The Fe^{2+} and Fe^{3+} are represented by 2 and 3, respectively.

	B site																Fe^{3+} surroundings	
Model	1	2	3	4	5	6	7	8	9	10	11	12	13	14	15	16	*A* plane	*B* plane
1	3	2	2	2	3	2	3	3	2	2	3	2	3	3	2	3	$N2,N3\pm$	$N1,N4\pm$
2	3	2	2	2	3	2	3	3	2	3	2	2	3	3	3	2	$N2,N3\pm$	$N1,N4\pm$
3	3	3	3	2	3	2	2	2	2	3	3	3	3	2	2	2	$N1,N4\pm$	$N3\pm$
4	3	3	3	2	3	2	2	2	3	3	3	2	2	3	2	2	$N1,N4\pm$	$N2,N3\pm$
5	3	2	2	3	2	2	3	3	2	2	3	3	3	2	2	3	$N4\pm$	$N4\pm$
6	3	2	3	2	3	2	3	2	3	2	3	2	3	2	3	2	$N2,N3\pm$	$N2$
7	3	2	2	3	2	2	3	3	3	2	3	2	3	2	3	2	$N2,N3\pm,N4\pm$	$N2,N3\pm,N4\pm$
8	3	3	2	2	3	2	3	2	3	2	3	2	3	3	2	2	$N2,N3\pm,N4\pm$	$N2,N3\pm,N4\pm$
9	3	2	3	2	2	3	3	2	3	2	2	3	3	2	3	2	$N2,N3\pm,N4\pm$	$N2,N3\pm,N4\pm$
10[a]	2	2	2	2	3	3	3	3	2	2	2	2	3	3	3	3		$N1$
11[a]	3	3	3	3	2	2	2	2	3	3	3	3	2	2	2	2	$N1$	

[a]Verwey model.

the magnetic interaction. These are shown in Fig. 6. We label them $N1$, $N2$, $N3+$, $N3-$, $N4+$, and $N4-$. Here $N3+$ is related to $N3-$ by a mirror operation, as is $N4+$ to $N4-$. The nearest-neighbor configurations on the A and B planes for each model are listed in Table II. Since the same Fe^{3+} nearest-neighbor configurations on the A and B planes differ by 90°, they must be counted as different sites. From Table II, we see that several models have five or more different Fe^{3+} sites. Using some additional assumptions, Mizugouchi[14] proposed that one of the five Fe^{3+} is on the A plane and other four are on the B plane. However, from Table II, none of the models satisfy this condition. Since Cc symmetry has been clearly established by several experiments, Mizugouchi's assumptions must be seriously questioned.

IV. EXPERIMENT

We used electron diffraction to check the charge-ordering models listed in Table II. The technique we used is convergent-beam electron diffraction (CBED). Compared to the use of point diffraction patterns (with plane-wave incidence), CBED has two important advantages (1) a small focused probe, and (2) it provides intensity versus incident-angle information. The first advantage enables us to study a perfect crystal from a nanometer size area, while the second advantage gives rocking curve information. This is important, since the electron-diffraction intensity strongly depends on incident-beam direction through dynamical diffraction.

A Philips EM400T transmission electron microscope was used, with an incident electron energy of 100 kV. The specimen was a polycrystalline body of Fe_3O_4 prepared by sintering Fe_3O_4 powder at 1500 °C in a Ar-O_2 flowing gas environment for 24 h. The oxygen partial pressure was set at $10^{-3.5}$ atm O_2 corresponding approximately to an equilibrium O:Fe stoichiometry of 4:3.[32] The sample was cooled to room temperature in about 3–4 min. As with many metal oxides, it was expected that a minor amount of oxidation could occur upon cooling in an atmosphere of constant oxygen partial pressure. However, x-ray diffraction and optical microscope indicated that no additional phases were present such as Fe_2O_3. The sample was concluded to be nearly stoichiometric Fe_3O_4 and phase pure. The cation impurity content was analyzed by semiquantitative spectrochemical analysis, where the major impurities, Mn and Ni, were each found at 10–100 ppm level, and Al, Ca, Cu, Mg, and Si were each found at 1–10 ppm level. The typical crystal grain size was about 100 μm within the polycrystalline microstructure. A transmission sample was prepared by chemical etching with 80% phosphoric acid (H_3PO_4) and 20% water at a temperature of about 120 °C. The sample was mounted in a Gatan double tilt, liquid-helium goniometer stage, and cooled by liquid nitrogen to 90 K. The sample was cooled in the presence of the magnetic field of the objective lens of the microscope, which ensures that the c axis (the magnetic easy axis) is close to the beam direction. Figure 4 shows a CBED pattern of low-temperature magnetite close to the [001] zone axis direction, obtained with a probe size of about 1000 Å, which clearly shows several low-order reflections and a characteristic first-order Laue zone ring (FOLZ) due to the doubling of the c axis. The pattern was recorded on film. There are two types of twins in low-temperature magnetite, one is c-axis twinning about the b axis with zigzag c axis and the other is a-b twinning about the c axis with a and b axes interchanged. Figure 4 is taken from a single domain of size 4 μm. The second type of twin can be imaged when viewing close to the [001] zone axis. The first type of twin cannot be imaged close to the [001] zone axis, however, when it does occur the FOLZ in Fig. 4 disappears. This effect is observed in our experiments.

The reflections in Fig. 4 can be divided into strong reflections and weak reflections. The weak ones disappear above the transition temperature, so they are also called the low-temperature reflections. This is clearly seen in our experiments, where they switch on and off across the transition temperature. From the extinction conditions given in Sec. II, the kinematically allowed reflections in the zero-order Laue zone (ZOLZ) above the transition temperature are $g=n(4,0,0)+m(0,4,0)$ (monoclinic index), with n,m integers, or $g=n(2,2,0)+m(2,\bar{2},0)$ in cubic indices. These reflections are the strong reflections in Fig. 4 and they form a lattice. Hence, kinematically forbidden reflections in the [001] ZOLZ such as (200) are also dynamically forbidden above the transition temperature, if the weak second-order Laue zone interactions are neglected. For those low-temperature reflections that are otherwise forbidden above the transition temperature, their structure factors and intensities are very sensitive to the low-temperature charge ordering or atomic displacements or both. Specifically, the low-order reflections are more sensitive to charge ordering than the high-order ones, and

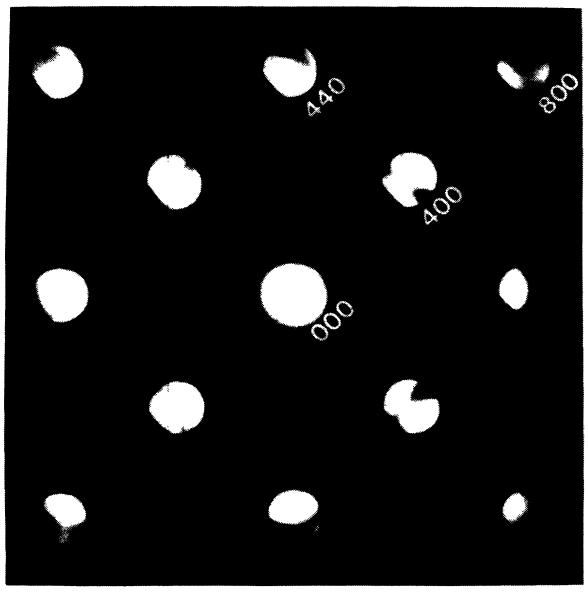

FIG. 7. Large camera length, short exposure time diffraction pattern corresponding to Fig. 4. This pattern shows the details of the intensity variation in the CBED disks of high-temperature reflections.

the low-temperature reflections in the first-order Laue zone (FOLZ) outer ring are most sensitive to atomic displacements.

V. MODEL COMPARISON

The [001] zone axis is chosen experimentally because several low-order reflections in this zone axis are model sensitive, especially the (±200) reflections. Table III lists the electron and x-ray structure factors for several low-order reflections in the [001] zone axis. The structure factors are calculated with the atomic positions and Debye-Waller factors listed in Table I,[13] the x-ray atomic scattering factors of Fe^{2+} and Fe^{3+} are those for spherical ions from Table 2.2B of the *International Tables for X-Ray Crystallography*,[33] and the atomic scattering factors for O^{2-} are taken from Sanger.[34] These are calculated from the O^{2-} wave function of the "2+ well" model of Watson.[35] The electron atomic scattering factor is obtained from the Mott formula

$$f^{\mathrm{el}}(s)=\frac{m_e e^2}{8\pi\varepsilon_0 h^2}\frac{Z-f^x(s)}{s^2} \tag{4}$$

in the usual symbols.[36]

From Table III, using the (400) structure factor, we see that the models can be divided into three groups, which corresponds to our 1-3, 3-1, and 2-2 fillings. The (020) structure factor is approximately constant, while (200) has two very different values, 0.1 and 0.48 V, except for model 6. The (130) and (310) structure factors differ from one model to another in a more complicated way. The (200) and (020) amplitudes can be understood as follows. In general, the structure factors for the $(h00)$ and $(0h0)$ reflections are given by

$$F(h00)=2[1+\exp(\pi ih)]\sum_{i=1}^{16} f_i\exp(2\pi ihx_i)\ , \tag{5}$$

$$F(0h0)=2[1+\exp(\pi ih)]\sum_{i=1}^{16} f_i\cos(2\pi hy_i)\ . \tag{6}$$

If we neglect the small low-temperature atomic displacements, the sixteen independent B-site positions are given as follows:

$$x=0.125+0.25(i-1),\ y=0.25 \quad \text{for } i=1\text{–}4\ ,$$

$$x=0,\ y=0.125+0.25(i-5) \quad \text{for } i=5\text{–}8\ ,$$

$$x=0.125+0.25(i-9),\ y=0 \quad \text{for } i=9\text{–}12\ ,$$

$$x=0.25,\ y=0.125+0.25(i-13) \quad \text{for } i=13\text{–}16\ .$$

For the (020), from the above and Eq. (6), the total contribution to $F(020)$ from charge-ordering is zero, because for positions $i=5$–8 and $i=13$–16, $\cos(4\pi y_i)=\pm\cos(\pi/2)=0$ and $\cos(4\pi y_i)=-1$ for $i=1$–4 but is equal to 1 for $i=9$–12, giving a zero total. Hence the contribution to $F(020)$ in Table III is mostly due to the low-temperature atomic shifts. For (±200), the contributions from positions $i=5$–8 and 13–16 cancel out, leaving remaining contributions from positions $i=1$–4 and 9–12. This contribution is zero for models 2, 3, and 5, but nonzero for the other models. Hence we conclude that the (±200) structure factor is very model dependent, whereas the (020) is very model independent.

Table III also reveals the increased sensitivity of electron diffraction to charge ordering by comparison with x rays. The model 1 (200) electron structure factor is about 15 times larger than the corresponding x-ray one, if the high-temperature (400) reflection is used as a reference. So the intensity of this beam is about 200 times stronger in electron diffraction than in x rays. This sensitivity is mainly due to the factor $1/s^2$ in the Mott formula [Eq. (4)].

In the Introduction we emphasized that the diffracted electron intensity is not simply related to structure factor amplitude due to strong dynamical diffraction. Thus dynamical calculations are required for the different models for comparison with experiment. The dynamical theory of transmission electron diffraction for a parallel sided crystalline slab traversed by a collimated electron beam is now well established (for a review, see Ref. 36). If backscattering is neglected (a good approximation for beam energies above a few kV), the required solution of the one-electron Schrödinger equation leads to an eigenvalue equation of the form

$$2KS_gC_g+\sum_h U_{gh}C_h=2K_n\gamma C_g\ , \tag{7}$$

TABLE III. Electron structure factor amplitude ($|V(hkl)|$ in V) listing of several low-order reflections for models 1–9 in Table II. For comparison, we also listed the x-ray structure factors ($|F(hkl)|$ in number of electrons per cell) of (200), (020), and references reflection (400). For other details, see text.

Model	1	2	3	4	5	6	7	8	9
$\|V(110)\|$	0.0161	0.0116	0.0222	0.0192	0.0173	0	0.0166	0.0276	0.0141
$\|V(200)\|$	0.4821	0.1007	0.1090	0.4839	0.1049	0.9488	0.4829	0.4828	0.4832
$\|V(020)\|$	0.2587	0.2858	0.2616	0.2345	0.2454	0.3020	0.2725	0.2749	0.2725
$\|V(130)\|$	0.1505	0.1464	0.1592	0.1553	0.2185	0	0.0126	0.0056	0.2138
$\|V(310)\|$	0.1505	0.1521	0.1474	0.1492	0.2170	0	0.0044	0.0024	0.2066
$\|V(400)\|$	0.3149	3.149	2.847	2.847	2.998	2.998	2.998	2.998	2.998
$\|F(200)\|$	6.885	0.1435	0.0226	6.883	0.0830	13.77	6.881	6.881	6.886
$\|F(020)\|$	11.66	11.27	11.62	12.02	11.86	11.03	11.46	11.43	11.46
$\|F(400)\|$	653.4	653.4	671.0	671.0	662.2	662.2	662.2	662.2	662.2

giving n eigenvalues $\{\gamma^i\}$ and n eigenvalues $\{C_g^i\}$. Here $2KS_g = K^2 - (\mathbf{K}+\mathbf{g})^2$ is the excitation error for reflection g, which depends on the incident-beam direction. We do not assume that the crystal possesses a center of symmetry. The intensity of a beam diffracted by a slice of thickness t is given by

$$I_g = \left| \sum_i C_0^{i\,-1} C_g^i \exp(2\pi i \gamma^i t) \right|^2 . \tag{8}$$

Here C_0^{-1} is the first row of the inverse of the eigenvector matrix. The computer program we have used to evaluate these expressions (modified to accommodate the large unit cell and number of beams) has been published.[37] The parameters used in a dynamical diffraction simulation are the crystal thickness, the beam direction, an "optical" potential for the crystal (real and imaginary parts) and the incident-beam energy. The beam energy is known *a priori* with sufficient accuracy in this case (100 kV). The imaginary part of the real-space potential is used to take account of the effects of energy loss from the beam due to inelastic scattering. The Fourier coefficients of this "absorption potential" must be found by experiment. The importance of this imaginary potential varies, and will be discussed later. The beam direction and sample thickness can be measured accurately from the strong high-temperature reflections such as (400), (440), and (800), shown in Fig. 7, which is recorded with shorter exposure time than Fig. 4. To a good approximation, they are model insensitive, and the effects of the low-temperature reflections can be neglected. In contrast to the refinement procedures we used in our measurements of the GaAs structure factors, we have used a "whole-pattern" matching procedure in this case. The intensity distributions (rocking curves) in the (440) and (800) reflections are found to be very sensitive to thickness and to the beam direction, which can therefore be measured rather accurately by matching the experimental patterns in the CBED disk to calculations. Figure 8 shows the result of our refinement of Fig. 7. The thickness was found to be 400±10 Å and the incident-beam direction was measured with an accuracy of 0.015 of the $g(200)$ reciprocal-lattice vector. Mössbauer and NMR measurements on Fe^{2+} and Fe^{3+} strongly indicate that magnetite is an ionic crystal. For the strong reflections, the difference between neutral and ionic atoms potentials is small and was not detectable using our refinement procedure. However, the difference between ionic and neutral potentials, especially the difference between the Fe^{2+} and Fe^{3+} scattering factors, is important for those low-temperature reflections that are sensitive to charge ordering. We have used atomic scattering factors for Fe^{2+} and Fe^{3+} from the international tables for x-ray crystallography, and O^{2-} scattering factors from Sanger[34] who used the "2+ well" O^{2-} model of Watson.[35] This particular O^{2-} scattering factor has been chosen because it, together with the Mg^{2+} scattering factor from the international tables, gives the best agreement with our accurately measured MgO low-order structure factors[38] from among all existing scattering factors. (This includes those based on neutral atoms. For a listing of these scattering factors see

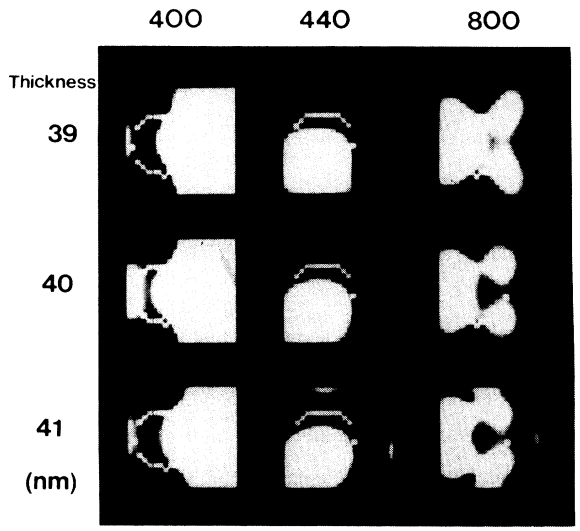

FIG. 8. Thickness and incident-beam direction refinement based on Fig. 7. A thickness of 40 nm gives the best agreement, and the (800) reflection is most sensitive to thickness. The position of the CBED disk is indicated by the superimposed open circle. This position gives the incident-beam direction.

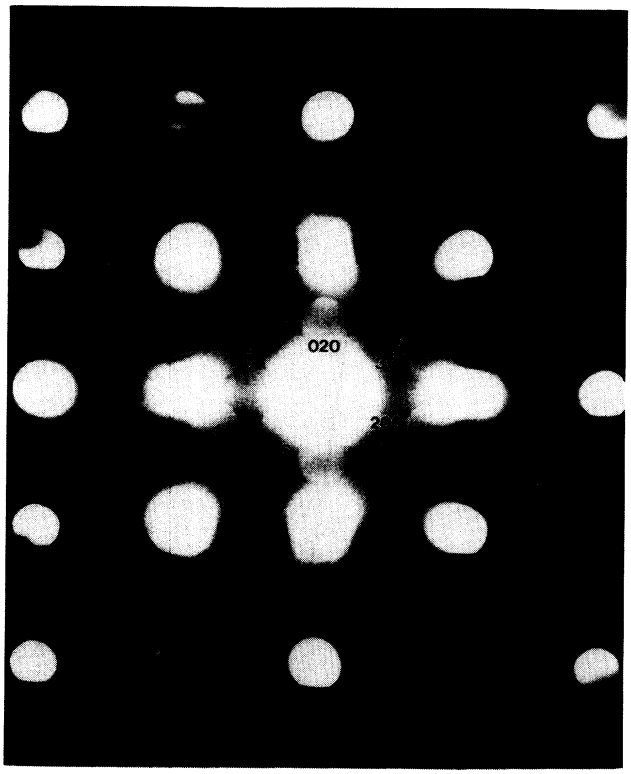

FIG. 9. The positions of the six points in the CBED disks, which were used for model comparison. This figure corresponds to Fig. 4, with a larger camera length. The most important feature in this figure is the asymmetry between the intensity of the (±200) and (0±20) reflections.

TABLE IV. Model and experimental intensity comparison for points 1–6 in Fig. 9. The intensity is normalized to point 1 for points 1–3 and to 4 for points 4–6.

Model	1 (020)	2 (−200)	3 (200)	χ^2	4 (−310)	5 (−1–30)	6 (3–10)	χ^2
1	100	304±46	218±58	20				
2	100	39.8±8.9	22.9±5.5	1.1	100	56.7±7.7	31±16	0.39
3	100	37.4±7.6	24.5±4.1	1.8	100	171±27	45±21	5.7
4	100	298±39	173±32	30				
5	100	31.1±7.0	5.1±1.8	6.5	100	83±12	25±13	0.8
6	100	680±110	407±78	28				
7	100	367±94	168±52	9.4				
8	100	358±88	170±51	10				
9	100	239±24	77±22	30				
exp	100	55.5±6.3	21.3±6.2		100	68±15	42±1	

Ref. 34.) The dynamical diffraction corresponding to Fig. 4 for different charge-ordering models was simulated using 97 beams, 60 of which are low-temperature reflections. The number of beams was chosen so that the addition of more beams did not significantly alter our results. The thickness and beam direction was taken from the refinement of Fig. 8. Absorption was not included, the effects of which will be discussed later.

The experimental intensity was recorded on film, then digitized into a computer using a charge-coupled-device (CCD) camera. As seen in Fig. 4, the weak low-temperature reflections sit on an inelastic background due to the strong reflections. This makes intensity measurement very difficult. To avoid this difficulty, we have selected a point near the edge of the CBED disk for several model-sensitive reflections for comparison with calculations based on different models. The background intensity for these points can be measured accurately by measuring the intensity outside the CBED disk. The position of these points is shown in Fig. 9. The measured intensities of points 1–6 in Fig. 9 are listed in Table IV. Figure 10 shows one example of these intensity measurements. Since the beam direction has been accurately measured, these points are well-defined quantities (recall that one point in a CBED disk corresponds to a particular incident-beam direction). The intensities at these points for the different models were calculated as described above; the results have been normalized and are shown in Table IV. The intensities were normalized to point 1 for points 1–3 and to point 4 for points 4–6. The different normalization was used because of the uncertainty in the absorption potential, which will be discussed further in the Sec. VI. From Table IV, we see that there are large intensity differences at points 1, 2, and 3 [reflections (020), (−200), and (200)] for the different charge-ordering models. Models 2 and 3 give the best agreement. The other models have very large χ values and may be excluded. Models 2 and 3 are distinguished by the intensities of points 4, 5, and 6 [reflections (−310), (−1–30), and (3–10)]. Model 2 clearly gives better agreement than model 3. Hence we conclude that charge-ordering model 2 gives the best agreement with the CBED experimental results.

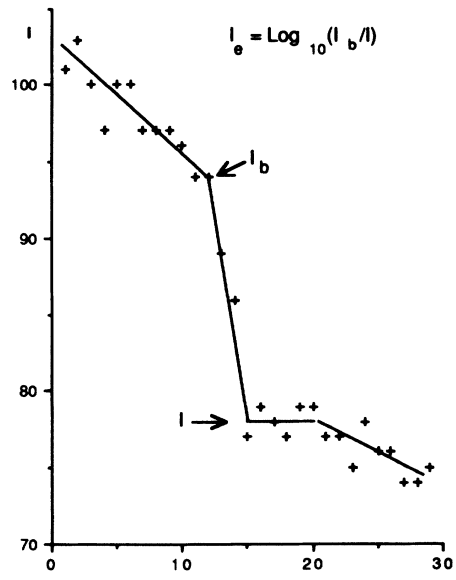

FIG. 10. Intensity measurement at point 2 in Fig. 9. The intensity profile is taken along [010] through point 2. The intensity in this figure is the optical transmission intensity of the electron micrograph, as detected by a CCD camera. The logarithm of the ratio I_b/I shown in this figure gives the electron intensity at point 2 minus the inelastic background.

VI. DISCUSSION

Before discussing the implications of model 2 as the best model, we consider some of the uncertainties associated with our experiment and their possible effects on our conclusion.

(1) Errors in thickness and beam direction. The error in thickness determination is 1 nm and the error in the beam direction is about 0.015 of $g(200)$. The error in intensity due to these two combined errors can be found using simulations. The error listed in Table II is due to these two errors.

(2) Errors due to the use of an insufficient number of beams N. The simulation was carried out using 93 beams. The computer time for the Bloch wave method is proportional to N^2, which is the main limitation on N

(typical times on our VAXstation 3200 were 26 sec per data point for $N=93$) (i.e., per incident-beam direction). The error caused by this is about one fifth of the errors due to the thickness and beam direction, which can be neglected.

(3) Errors in the absorption potential. The absorption potential is an unknown quantity in electron diffraction. Despite theoretical effort,[39,40] the most reliable estimates of the absorption potential come from accurate experimental measurements. The importance of the absorption potential varies and depends on the required experimental accuracy. In our accurate measurements of structure factors in GaAs (1% accuracy) we found that the absorption potential must be included and refined as an independent parameter. However, the accuracy of this experiment is only about 20%. To estimate the effect of the neglect of the absorption potential, we used absorption coefficients $V_g'=0.05V_g$ in our simulations, following a widely used rule of thumb.[36] The phase of the absorption potential was neglected, since the absorption is mostly due to the high-temperature cubic structure that is centrosymmetric. We found that this absorption potential does not change the intensity ratios between the (020), (−200), and (200) reflections, or those between the (−310), (−1–30), and (3–10). However, it does change the ratios between these two groups. We also found that if we normalize these intensities to a single reflection such as the strong (020), the simulation without absorption gives better agreement than with an overall absorption factor of 0.05. This absorption effect can be readily understood. The most important absorption coefficients are those of the high-temperature reflections, which couple the low-temperature reflections we are interested in. The arrangement of high-temperature couplings vector around the (200) type reflections is differnt from the that around the (130) type. For the (200) type reflections it is the (400) type couplings, and for the (130) type reflection it is the (400) and (440) type couplings. Hence absorption effects for the (200) type reflections are approximately the same, and these differ from those for the (130) type reflections. This can be understood as equivalent to different incident-beam directions. This is why different normalization was used for (200) type and (130) type reflections. Since the ratio of the same type reflections was used in this paper to check the models, absorption effects can be neglected to a good approximation.

(4) Errors in the atomic potential. The structure factor for low-order reflections can be written as follows:

$$F_g \sim c(f^{\mathrm{Fe}^{2+}}-f^{\mathrm{Fe}^{3+}})+\sum_i 2\pi i\mathbf{g}\cdot\Delta\mathbf{r}_i \ .$$

The first term is most sensitive to the difference between Fe^{2+} and Fe^{3+}, while the second term is due to the low-temperature atomic displacements. The actual charge difference between Fe^{2+} and Fe^{3+} ions in the crystal is an unknown quantity, although that they are clearly distinguished in Mössbauer experiments. If the difference between them is very small then the difference between different charge-ordering models is also small. To test the effects of different valences of Fe ion on our results, we tried using 0.25 electrons on the Fe^{2+} site and 0.75 electrons on the Fe^{3+} site by taking

$$f(\mathrm{Fe}^{2.25+})=f(\mathrm{Fe}^{2+})+0.25[f(\mathrm{Fe}^{3+})-f(\mathrm{Fe}^{2+})] \ ,$$

$$f(\mathrm{Fe}^{2.75+})=f(\mathrm{Fe}^{3+})+0.25[f(\mathrm{Fe}^{2+})-f(\mathrm{Fe}^{3+})] \ .$$

We found that the conclusion that model 2 is the best model remained unchanged, however, the overall χ^2 value for model 2 increased from 1.5 to 4.4 and the χ^2 values for the other models with large χ^2 values are slightly decreased, but these χ^2 values are still larger than that for model 2.

(5) Errors in the atomic coordinates of the low-temperature structure. The atomic coordinates of the low-temperature magnetite structure have been measured by Iizumi *et al.*[13] These are approximate coordinates, due to their use of an incorrect (smaller) cell with higher symmetry in the refinement. (Their cell uses a and b axes with half the length of ours, with symmetry $Pmc2_1$.) Hence the contribution to reflections ($hk0$) with h and k all odd, such as (130) and (310), from atomic shifts is zero. The reason for this approximation is that these reflections are much weaker than other low-temperature reflections in neutron diffraction. This possible error does not affect our conclusions based on the (020) and (200) reflections, because their incorrect choice does not affect these reflections. However, it does make the difference between models 2 and 3 uncertain.

We conclude that, if the atomic coordinates of Iizumi *et al.*[13] are accepted, then model 2 and the full ionic potential give the best agreement to our experiment CBED results. Possible errors in the atomic coordinates make the choice of model 2 over model 3 somewhat uncertain. However, other models are ruled out based on the large χ^2 caused by the (200) reflections. The difference between models 2 and 3 consists of an interchange in the Fe^{2+} and Fe^{3+} occupancies.

Among the existing experimental results, Mizugouchi's NMR results[9] give the most direct information on charge ordering. However, since we have shown before that none of the models with Cc symmetry agree with Mizugouchi's assumption that one Fe^{3+} site is on an A plane and the other four are on the B plane. We feel that symmetry provides stronger evidence, which has been confirmed by several experiments. Model 2 has a total of six different Fe^{3+} sites, if we only consider the nearest-neighbor Fe^{3+} ions. Further work is needed to understand the inconsistency between these six sites and the five Fe^{3+} sites detected by Mizugouchi. Mössbauer experiments[7,8] have identified two different Fe^{2+} sites, however, model 2 gives five Fe^{2+} sites. Model 2 gives finite magnetic scattering into the (004) reflections due to the one and three Fe^{3+} ions in the A and B planes, respectively. This magnetic scattering was not detected by Shirane *et al.*[6] within their experimental error. The reason for this may be due to the a-b twinning, since the magnetic scattering from different domains differs by π and therefore cancels. It is now known that a-b twinning can be suppressed by cooling and squeezing in a magnetic field.[13] It would therefore be possible to test our model by remeasuring the magnetic (004) scattering. The model-2 charge ordering does have a center of symmetry

on B-site number 1, however, this center of symmetry is destroyed by the low-temperature atomic shifts. This may explain the magnetoelectric effects observed by Rado *et al.*[18] and Shiratori *et al.*[19]

The electrons on the B sites are localized, and below the transition temperature they form a regular lattice. Above the transition temperature they can be described as a "Wigner glass" of electrons in a localized, disordered state.[11] The high-temperature conductivity is due to electron hopping. Ihle and Lorenz[15] have proposed that $U \gg B$, where U is the nearest-neighbor Coulomb interaction and B is the bandwidth. In this limit of extreme localization, we may neglect quantum effects and treat the system classically. Then the Coulomb interaction energy of each electron with its neighboring electron can be calculated by methods similar to those used for the Madelung energy. Then

$$U=\frac{e^2}{4\pi\epsilon a}\sum_j \frac{n_j a}{r_j} .$$

Here a is the nearest-neighbor distance, ϵ is the dielectric constant, and n_j is the total number of electrons on the sphere of radius r_j. This energy diverges for an infinite number of electrons. To avoid this, we chose the high-temperature disordered phase as a reference, in which every B site is occupied by 0.5 electrons. Subtracting off this 0.5 electrons from the ordered structure, we have $+0.5$ and -0.5 electrons for every Fe^{3+} and Fe^{2+}, respectively. We can then calculate the electron correlation energy for each site from Iizumi

$$U=\frac{e^2}{16\pi\epsilon a}\sum_j \frac{(n_j^- - n_j^+)a}{r_j} . \quad (9)$$

Here n_j^+ and n_j^- are the number of Fe^{3+} and Fe^{2+} ions on sphere r_j, respectively. This series has been summed over a number of neutral shells in which there are equal numbers of Fe^{2+} and Fe^{3+} to avoid the Fe^{2+} and Fe^{3+} fluctuations at the cutoff sphere, so that the series converges fairly quickly. The high-temperature atomic coordinates are used because the uncertainty about the couplings of charge-ordering model and low-temperature atomic displacement. The computational results are shown in Table V. We find that the Verwey model has the overall lowest classical electron correlation energy, while models 2 and 3 are the second lowest. The difference between model 2 and model 3 are within our computational error. From Table V, the differences between different models (except the Verwey model) are small [on the order of $0.5e^2/(16\pi\epsilon a)$]. But the Verwey model has now been excluded by much experimental evidence, and hence the electron-phonon interaction must play an important role in stabilizing the structure. Thus the electron-phonon interaction energy must be larger than the difference between the Verwey model and our model 2. This is

$$\Delta E_{e\text{-ph}} > 1.8\frac{e^2}{16\pi\epsilon a} .$$

From Table V, each site in the unit cell has a slightly different electron correlation energy, which ranges from $-1.39e^2/(16\pi\epsilon a)$ to $-1.28e^2/(16\pi\epsilon a)$ for model 2. The electron on B plane has the highest energy. If we only count the nearest-neighbor interaction, the electron correlation energy due to short-range order is $U_1=-2e^2/(16\pi\epsilon a)$. Our calculations also show that the energy of one electron on the empty Fe^{3+} site has significantly higher energy than the occupied site (Fe^{2+} site), for model 2 the Fe^{3+} site energy ranges from $1.30e^2/(16\pi\epsilon a)$ to $1.38e^2/(16\pi\epsilon a)$ for the various empty sites.

It has been postulated that the low-temperature magnetite structure results from the condensation of a phonon coupled charge-density wave. Model 2 shows such a charge-density wave. In Fig. 11, we have linked the nearest-neighbor electrons and see that the form a three-dimensional (3D) wave string with $\mathbf{k}=2\pi(1/2a,0,1/c)$, polarized in the b direction. This wave character becomes clearer in the projection of the 3D wave string onto the a-b plane shown in Fig. 11.

TABLE V. Electron correlation energy [in units of $e^2/(16\pi\epsilon a)$, $a=2.9685$ Å] for different charge-ordering models and different electrons in the unit cell. There are 15 different B sites in the unit cell and eight of them are occupied by electrons. The correlation energy for these eight electrons and the total correlation energy in the unit cell are listed in this table in the order of their site number in Table II.

	Electron correlation energy for electron No.								
Model	1	2	3	4	5	6	7	8	Total
1	−1.35	−1.33	−1.35	−1.27	−1.35	−1.35	−1.35	−1.28	−42.58
2	−1.39	−1.30	−1.39	−1.28	−1.39	−1.39	−1.31	−1.28	−42.81
3	−1.30	−1.38	−1.32	−1.35	−1.31	−1.38	−1.32	−1.35	−42.84
4	−1.24	−1.39	−1.32	−1.35	−1.28	−1.39	−1.35	−1.32	−42.58
5	−1.30	−1.30	−1.30	−1.30	−1.31	−1.31	−1.31	−1.31	−41.74
6	−1.31	−1.31	−1.36	−1.36	−1.31	−1.31	−1.36	−1.36	−42.66
7	−1.24	−1.33	−1.30	−1.30	−1.35	−1.35	−1.35	−1.35	−42.33
8	−1.33	−1.24	−1.35	−1.35	−1.35	−1.35	−1.30	−1.30	−42.33
9	−1.35	−1.35	−1.31	−1.31	−1.28	−1.34	−1.33	−1.36	−42.54
10[a]	−1.39	−1.39	−1.39	−1.39	−1.39	−1.39	−1.39	−1.39	−44.60

[a]Verwey model.

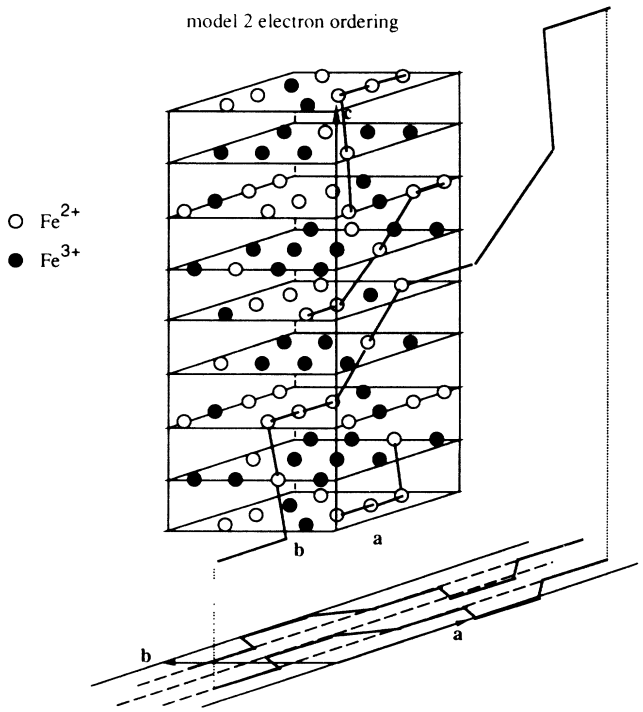

FIG. 11. Model 2 electron ordering, and the resulting charge-density wave. The nearest-neighbor Fe^{2+} ions are linked by strings and form a wave with polarization direction along the *b* axis. This wave character is seen clearly in a projection onto the *a-b* plane.

VII. CONCLUSIONS

We conclude this paper with the following three points: (1) Diffraction experiments have clearly established that the low-temperature structure of magnetite has *Cc* symmetry (monoclinic). With this *Cc* symmetry and under the "Anderson condition," we show that there are ten independent charge-ordering models, including the Verwey model. Previous experimental evidence rules out the Verwey model, but cannot distinguish between the other nine models.

(2) Our comparison between experimental CBED patterns at the [001] zone axis and simulated CBED patterns for different charge-ordering models using existing atomic coordinates and an ionic potential shows that our "model 2" gives the best agreement, while model 3 is the second best. Our use of approximate atomic coordinates, derived from the work of Iizumi *et al.*,[13] makes the difference between models 2 and 3 somewhat uncertain. Other models, however, are definitely ruled out by the difference between the (200) and (020) intensities observed in our experiments. Both model 2 and model 3 show a characteristic charge-density wave. The difference between model 2 and model 3 consists of an interchange in the Fe^{2+} and Fe^{3+} *B*-site occupancies of the spinel lattice.

(3) Our classical electron correlation energy calculations show that the Verwey model has the lowest electron correlation energy, while our models 2 and 3 are the second lowest. This indicates the importance of the electron-phonon interaction in this system.

This work on the low-temperature structure of magnetite forms an essential preliminary to research into the atomic mechanism responsible for the metal-insulator transition in this material by high-resolution electron microscopy.

ACKNOWLEDGMENTS

This work was made possible by The National Science Foundation (NSF) Grant No. DMR8813879 (J.C.H.S., P.I.) and the resources of the Arizona State University NSF National Center for High resolution electron microscopy. We are most grateful to Dr. M. O'Keeffe for many enlightening discussions.

[1]E. J. W. Verwey and P. W. Haayman, Physica (Utrecht) **8**, 979 (1941).
[2]E. J. W. Verwey, P. W. Haayman, and F. C. Romeijan, J. Chem. Phys. **15**, 181 (1947).
[3]W. C. Hamilton, Phys. Rev. **110**, 1050 (1958).
[4]T. Yamada, K. Suzuki, and S. Chikazumi, Appl. Phys. Lett. **13**, 172 (1968).
[5]E. J. Samuelson, E. J. Bleeker, L. Dobrzynski, and T. Rise, J. Appl. Phys. **39**, 1114 (1968).
[6]G. Shirane, S. Chikazumi, J. Akimitsu, K. Chiba, M. Matsui, and Y. Fuji, J. Phys. Soc. Jpn. **47**, 1779 (1975).
[7]R. S. Hargrove and W. Kundig, Solid State Commun. **8**, 303 (1970).
[8]M. Rubinstein and D. W. Forester, Solid State Commun. **9**, 1675 (1971).
[9]M. Mizugoucyi, J. Phys. Soc. Jpn. **44**, 1501 (1978); **44**, 1512 (1978).
[10]Y. Fuji, G. Shirane, and Y. Yamada, Phys. Rev. B **11**, 2036 (1975).
[11]N. F. Mott, Metal-Insulator Transitions (Taylor & Francis, London, 1974); Philos. Mag. B **42**, 327 (1980).
[12]Y. Yamada, in *Experiments on High Energy Particle Collisions, 1973 (Vanderbilt Conference)*, Proceedings of the International Conference on New Results from Experiments on High Energy Particle Collisions, AIP Conf. Proc. No. 12, edited by R. S. Parvini (AIP, New York, 1973).
[13]M. Iizumi, T. F. Koetzle, G. Shirane, S. Chikazumi, M. Matsui, and S. Todo, Acta Crystallogr. Soc. B **38**, 2121 (1982).
[14]S. Iida, Philos. Mag. B **42**, 349 (1980).
[15]D. Ihle and B. Lorenz, Philos. Mag. B **42**, 337 (1980).
[16]J. Yoshida and S. Iida, J. Phys. Soc. Jpn. **42**, 230 (1977).
[17]M. Iizumi and G. Shirane, Solid State Commun. **17**, 433 (1975).
[18]G. T. Rado and J. M. Ferrari, Phys. Rev. B **12**, 5166 (1975).
[19]K. Shiratori, E. Kita, G. Kaji, A. Tasaki, S. Kimura, I. Shindo, and K. Kohn, J. Phys. Soc. Jpn. **47**, 1779 (1977).
[20]M. Tanaka, *Proceedings of the 45th EMSA*, edited by G. Bailey (San Francisco Press, San Francisco, 1987), p. 20.
[21]P. W. Anderson, Phys. Rev. **102**, 1008 (1956).
[22]J. M. Zuo, J. C. H. Spence, and W. Petuskey, in *Proceedings of*

the XIIth International Congress for Electron Microscopy, edited by G. B. Bailey (San Francisco Press, San Francisco, 1990), Vol. 2, p. 508.
[23]J. M. Zuo, J. C. H. Spence, and M. O'Keefe, Phys. Rev. Lett. **61**, 353 (1988).
[24]J. M. Cowley, Prog. Mater. Sci. **13** (1967).
[25]R. Wyckoff, *Crystal Structures* (Krieger, Malabar, Florida, 1965), Vol. 3, p. 79.
[26]J. Yoshida and S. Iida, J. Phys. Soc. Jpn. **47**, 1627 (1979).
[27]J. Gjonnes and A. F. Moodie, Acta Crsytallogr. **19**, 65 (1965).
[28]L. Pauling, *The Nature of the Chemical Bond,* 3rd ed. (Cornell University Press, Ithaca, New York, 1960).
[29]M. O'Keeffe (private communication).
[30]M. Rosenberg and H. Franke, Philos. Mag. B **42**, 419 (1980).
[31]T. E. Whall, Philos. Mag. B **42**, 423 (1980).
[32]R. Dieckmann, Ber. Bunsenges. Phys. Chem. **86**, 112 (1982).
[33]*International Tables for X-Ray Crystallography,* edited by J. A. Ibers and W. C. Hamilton (Kynoch, Birmingham, 1974), Vol. 4, Table 2.2B.
[34]P. L. Sanger, Acta Crystallogr. Sect. A **25**, 594 (1969).
[35]R. E. Watson, Phys. Rev. **111**, 1108 (1958).
[36]C. J. Humphrey, Rep. Prog. Phys. **42**, 1825 (1979).
[37]J. M. Zuo, K. Gjonnes, and J. C. H. Spence, J. Electron Microsc. Technol. **12**, 29 (1989).
[38]J. M. Zuo, J. C. H. Spence, J. Foley, and M. O'Keeffe, in *Acta-Scripta Metallurgica Proceedings Series,* edited by M. Ruhle *et al.* (Pergamon, New York, 1990), Vol. 4, p. 45.
[39]G. Radi, Acta Crystallogr. Sect. A **26**, 41 (1970).
[40]D. M. Bird and Q. A. King, Acta Crystallogr. Sect. A **46**, 202 (1990).

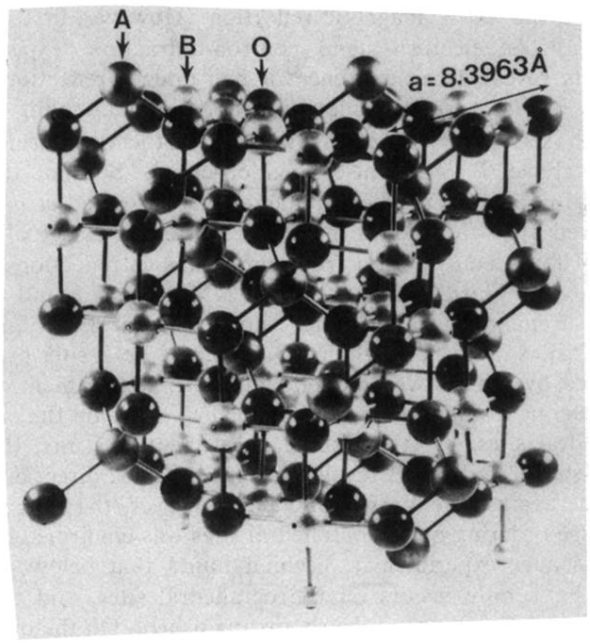

FIG. 1. Model of the spinel structure. This model contains one cubic unit cell. The *A* site, *B* site, and oxygen in this model are indicated by arrows.

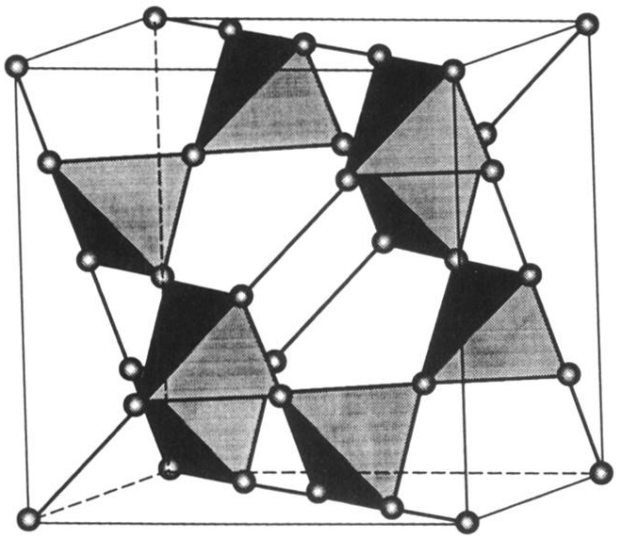

FIG. 2. The *B*-site structure of spinel structure. The *A* site and oxygen are not shown. The nearest-neighbor *B* sites form a tetrahedron. These tetrahedra are linked together by alternate corners, and the centers of the tetrahedra form a diamond lattice. The nearest-neighbor *B* sites form a string in ⟨110⟩ directions.

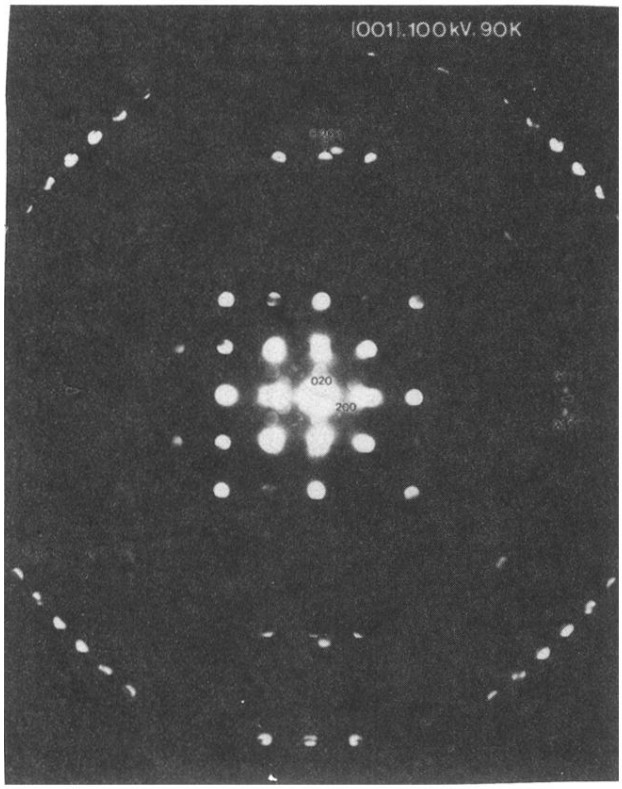

FIG. 4. Convergent-beam electron diffraction pattern of low-temperature magnetite near the [001] zone axis. This CBED pattern was recorded at 100 kV with a sample temperature of 90 K. The $(2n+1,00)$ and $(0,2n+1,0)$ reflections are missing, indicating c centering. The first-order Laue zone due to c-axis doubling is shown. The missing $(\pm 20,0,1)$ reflections due to the c glide are indicated by arrows.

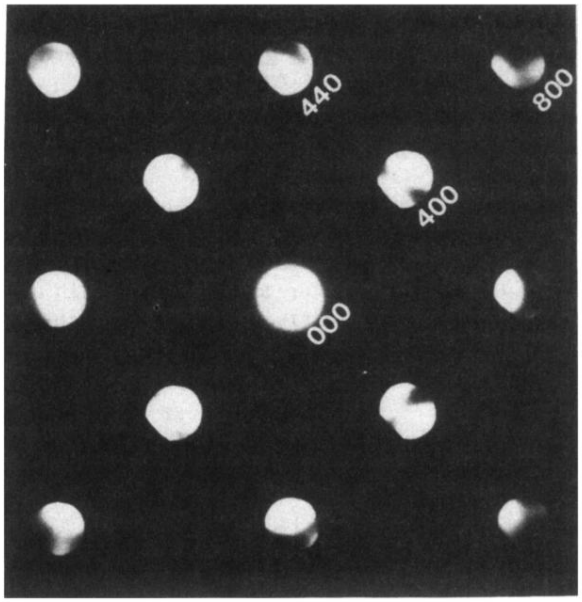

FIG. 7. Large camera length, short exposure time diffraction pattern corresponding to Fig. 4. This pattern shows the details of the intensity variation in the CBED disks of high-temperature reflections.

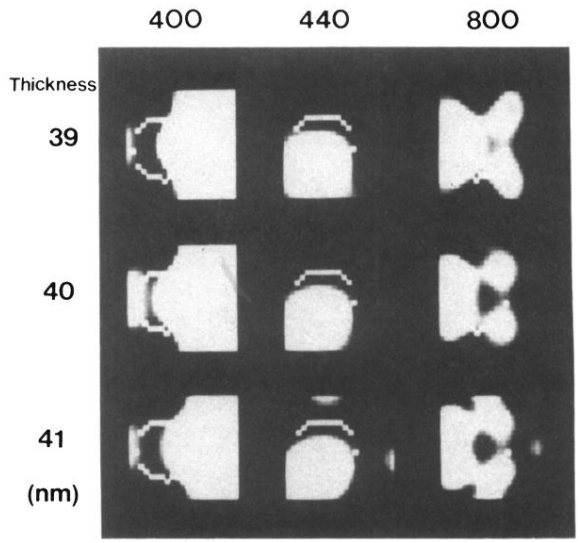

FIG. 8. Thickness and incident-beam direction refinement based on Fig. 7. A thickness of 40 nm gives the best agreement, and the (800) reflection is most sensitive to thickness. The position of the CBED disk is indicated by the superimposed open circle. This position gives the incident-beam direction.

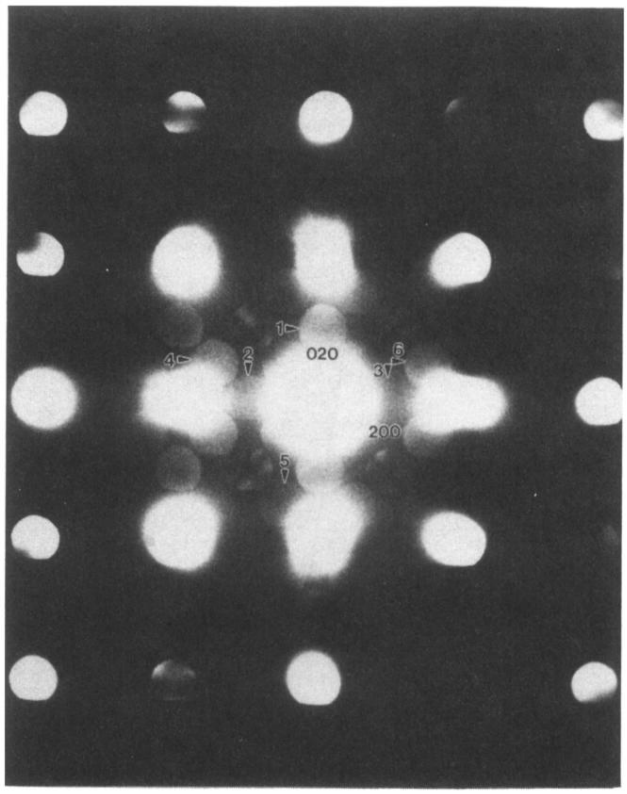

FIG. 9. The positions of the six points in the CBED disks, which were used for model comparison. This figure corresponds to Fig. 4, with a larger camera length. The most important feature in this figure is the asymmetry between the intensity of the ($\pm$200) and (0$\pm$20) reflections.